communications materials

ARTICLE

https://doi.org/10.1038/s43246-023-00364-5 OPEN

High proton conduction in Ba_2LuAlO_5 with highly oxygen-deficient layers

Riho Morikawa[1], Taito Murakami[1], Kotaro Fujii[1], Maxim Avdeev[1,2,3], Yoichi Ikeda[4], Yusuke Nambu[4,5,6] & Masatomo Yashima[1✉]

Proton conductors have found diverse applications, such as electrolytes in proton ceramic fuel cells, which require high ionic conductivity at low temperatures and high chemical stability. Here, we report the oxide, Ba_2LuAlO_5, which exhibits proton conductivities of 10^{-2} S cm^{-1} at 487 °C and 1.5×10^{-3} S cm^{-1} at 232 °C, high diffusivity and high chemical stability without chemical doping. Ba_2LuAlO_5 is a hexagonal perovskite-related oxide with highly oxygen-deficient hexagonal close-packed h′ layers, which enables a large amount of water uptake $x = 0.50$ in $Ba_2LuAlO_5{\cdot}x\ H_2O$. Ab initio molecular dynamics simulations and neutron diffraction show the hydration in the h′ layer and proton migration mainly around cubic close-packed c layers existing at the interface of octahedral LuO_6 layers. These results demonstrate that the high proton conduction allowed by the highly oxygen-deficient and cubic close-packed layers is a promising strategy for the development of high-performance proton conductors.

[1] Department of Chemistry, School of Science, Tokyo Institute of Technology, 2-12-1 W4-17 Ookayama, Meguro-ku, Tokyo 152-8551, Japan. [2] Australian Centre for Neutron Scattering, Australian Nuclear Science and Technology Organisation (ANSTO), Locked Bag 2001, Kirrawee DC, NSW 2232, Australia. [3] School of Chemistry, The University of Sydney, Sydney 2006, Australia. [4] Institute for Materials Research, Tohoku University, Sendai 980-8577, Japan. [5] Organization for Advanced Studies, Tohoku University, Sendai 980-8577, Japan. [6] FOREST, Japan Science and Technology Agency, Kawaguchi, Saitama 332-0012, Japan. ✉email: yashima@cms.titech.ac.jp

Safe and efficient power generation technologies using renewable sources are becoming increasingly important for sustainable energy development, with solid oxide fuel cells (SOFCs) based on oxide-ion conductors being a typical example[1–5]. However, the high operating temperature of conventional SOFCs (higher than 700 °C) has limited their applications in a wide range of fields at low and intermediate temperatures (300–600 °C). Since the activation energy for proton (H^+) conductivity is lower than that for oxide ion (O^{2-}) conductivity, proton conductors are known to exhibit higher conductivity than oxide-ion conductors at low temperatures[6–8]. Polymeric membranes such as Nafion and solid acid proton conductors such as $CsHSO_4$ show high conductivity near room temperature; however, they are chemically unstable and decompose at 100–200 °C[9–12]. In addition, materials that function at such low temperatures require expensive precious metal catalysts when used in fuel cells[12,13]. Some hydride (H^-) ion conductors show high conductivity at low temperatures[14–16]. However, they have drawbacks, such as being prone to decomposition at high temperatures or can only be synthesized by the high-pressure method[15,17].

In recent years, protonic ceramic fuel cells (PCFCs), which utilize proton-conducting ceramics, have been attracting attention as a technology alternative to SOFCs[7,18,19]. Proton-conducting oxides used in PCFCs are not only stable on heating but also have a lower operating temperature than SOFCs, enabling a stable energy supply at a lower cost[7,20–26]. To achieve high performance of PCFCs, high proton conductivity and high proton transport numbers are required. However, since proton conduction is dominated by the anion network, a limited number of structural types exhibit high proton conductivity, such as perovskites[27–31], layered perovskites[32–37], fluorite-type oxides[38,39], apatites[40], brownmillerites[41], fergusonites[42], and $La_{28-x}W_{4+x}O_{54+\delta}$[43]. Therefore, it is an important and challenging task to search for proton conductors belonging to other structure types.

A conventional strategy in the search for proton-conducting materials is the acceptor doping to form 'extrinsic oxygen vacancies' to allow hydration and obtain higher proton conductivity than that of the parent material[44,45]. The doping, however, often results in compositional inhomogeneity, reaction with electrode materials, proton trapping near dopants, and instability[46]. An alternative strategy is the search for a stable compound containing 'intrinsic oxygen vacancies' $V_{VO}^{\times}$, which enables hydration and proton conduction without the acceptor doping. Here, $V_{VO}^{\times}$ represents the vacancy V at the intrinsic oxygen vacant site VO using the Kröger–Vink notation. The intrinsic oxygen vacant site can be defined using the close-packed polytypes as follows. Crystal structures of many AMX_3 perovskites and perovskite-related compounds contain cubic and/or hexagonal close-packed AX_3 layers where the A and M are larger and smaller cations, respectively, and X is an anion. Intrinsically oxygen-deficient $AO_{3-\delta}$ layers are sometimes formed for the hexagonal and cubic close-packed layers (labeled h′ and c′, respectively), where δ is the amount of oxygen deficiency. Recently, perovskite-related oxides containing intrinsic oxygen vacancies have been reported to exhibit significant proton conduction without chemical doping (e.g., $Ba_5Er_2Al_2ZrO_{13}$[37], $Ba_5In_2Al_2ZrO_{13}$[47], $BaY_{1/3}Ga_{2/3}O_{2.5}$[48], and $Ba_7Nb_4MoO_{20}$[36]). Therefore, it is interesting to search for a material with a large number of intrinsic oxygen vacancies in its structure, which may show hydration and proton conduction without any chemical doping.

In this work, we searched for Ba_2BMO_5 compounds (B, M: cations) as candidates for proton conductors with intrinsic oxygen vacancies. The composition Ba_2BMO_5 (= $BaB_{1/2}M_{1/2}O_{2.5}$) has a lower oxygen content (5/6) compared with ABO_3 perovskite (1), and hence significant intrinsic oxygen vacancies are expected to exist in Ba_2BMO_5. To the best of our knowledge, we discovered a new material Ba_2LuAlO_5 through the search of Ba_2BMO_5 oxides (See the details in Supplementary Note 1 and Supplementary Fig. 1). Single-crystal and powder X-ray and neutron diffraction analyses reveal that Ba_2LuAlO_5 is a hexagonal perovskite-related oxide with highly oxygen-deficient h′ layers. In the present work, we report that the undoped Ba_2LuAlO_5 shows high bulk proton conductivity of 10^{-2} S cm^{-1} at 487 °C and 1.5×10^{-3} S cm^{-1} at 232 °C, which is higher than those of leading proton conductors. We also demonstrate that the hydration occurs in the h′ layer and that protons migrate mainly around cubic close-packed c layers existing at the interface of two octahedral LuO_6 layers. Therefore, the search for hexagonal perovskite-related oxides with both h′ and c layers would be a strategy to develop high-performance proton conductors.

Results and discussion

Synthesis and characterization of Ba_2LuAlO_5. Ba_2LuAlO_5 samples were prepared by solid-state reactions (See the details in "Methods"). The average grain and pore sizes were estimated to be 3.2(2) and 0.56(5) μm, respectively (Supplementary Fig. 2). The crystal structure of as-prepared Ba_2LuAlO_5 sample was successfully analyzed by the hexagonal $P6_3/mmc$ space group using the single-crystal X-ray diffraction (SCXRD) data (Supplementary Figs. 3 and 4; Supplementary Tables 1, 2 and 3). Details of the structure analysis are described in Supplementary Note 2. All the peaks in the X-ray powder diffraction (XRPD) pattern of as-prepared Ba_2LuAlO_5 were indexed to the primitive hexagonal lattice (Fig. 1a). Dry Ba_2LuAlO_5 samples were synthesized by annealing the as-prepared samples in vacuum at 800 °C. Rietveld refinements of the XRPD data for as-prepared Ba_2LuAlO_5 and neutron diffraction (ND) data for dry Ba_2LuAlO_5 were successfully carried out based on the hexagonal $P6_3/mmc$ Ba_2LuAlO_5 structure (Fig. 1b, Supplementary Fig. 5a, Supplementary Table 4). The bond valence sums of all the cations and anions for the refined structures of as-prepared and dry Ba_2LuAlO_5 are consistent with their formal charges,

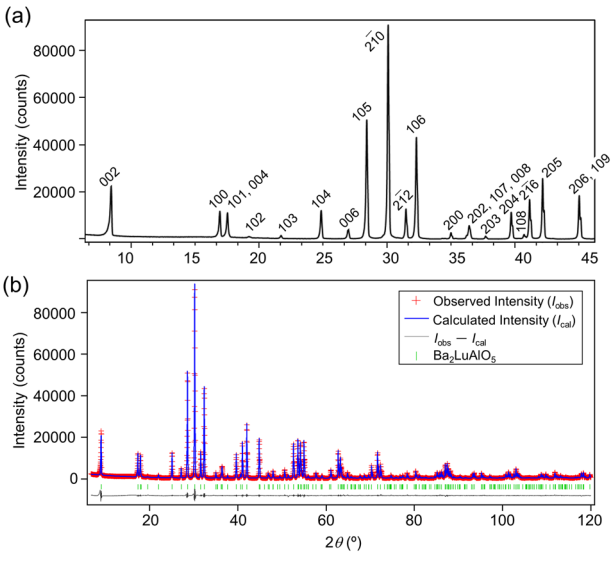

Fig. 1 Crystal structure analysis of as-prepared Ba_2LuAlO_5. a X-ray powder diffraction profile and **b** Rietveld pattern of as-prepared Ba_2LuAlO_5 at 22 °C ($R_{wp} = 0.084$). The red crosses, dark blue lines, and black dots represent observed, calculated, and difference intensities, respectively. Green ticks denote calculated Bragg peak positions of hexagonal Ba_2LuAlO_5.

demonstrating the validity of the refined crystal structures (Supplementary Tables 2 and 4).

Hydrated (deuterated) $Ba_2LuAlO_{4.52}(OD)_{0.96}$ samples were synthesized by annealing the as-prepared samples in D_2O saturated air. To investigate the atomic coordinates and occupancy of proton and oxide ions, ND data of the hydrated $Ba_2LuAlO_{4.52}(OD)_{0.96}$ sample were measured at 5 K. Rietveld refinements of ND data for the hydrated $Ba_2LuAlO_{4.52}(OD)_{0.96}$ were successfully carried out based on the hexagonal $P6_3/mmc$ Ba_2LuAlO_5 structure (Supplementary Fig. 5b, Supplementary Table 5). In preliminary analyses, the occupancy factors were found to be unity at all the cation sites and O1, O2, and O3 sites. The occupancy factors of Lu and Al atoms were refined to be 1 and 0, respectively, at the Lu site and 0 and 1, respectively, at the Al site, indicating complete Lu/Al occupational order. The oxygen 2*b* (0, 0, 1/4) site of hydrated $Ba_2LuAlO_{4.52}(OD)_{0.96}$ was found to split into the 6*h* (*x*, *x*/2, 1/4) O3 site with 1/3 occupancy, as in the case of as-prepared and dry Ba_2LuAlO_5, and $Ba_5Er_2Al_2ZrO_{13}$[37]. Extra oxygen atoms of $Ba_2LuAlO_{4.52}(OD)_{0.96}$ due to the hydration were located at the interstitial 2*c* (1/3, 2/3, 1/4) O4 site in the h′ layer, as observed in $Ba_5Er_2Al_2ZrO_{13}$ and $Ba_5Sc_{1.33}Al_2Zr_{1.67}O_{13.33}$[37,49]. The reliability factor for the structural model with the O4 atom $R_{wp} = 12.342\%$ was much lower than that without the O4 atom $R_{wp} = 18.352\%$. Further structure analyses of the ND data at 5 K on the basis of 416 models for the proton positions suggested four deuterium sites D1, D2, D3, and D4 (Supplementary Table 5), which is consistent with the probability density distribution of protons obtained by the ab initio molecular dynamics (AIMD) simulations (Supplementary Fig. 7). The average OD bond length 0.99(3) Å agrees with those from Raman spectra 0.98(4) Å (Supplementary Fig. 8) and IR spectra 0.99(4) Å (Supplementary Fig. 9). The lattice parameters *a* and *c* of hydrated $Ba_2LuAlO_{4.52}(OD)_{0.96}$ are 0.26% and 0.82% larger than those of dry Ba_2LuAlO_5, respectively, at 5 K, which is attributable to the water incorporation. The final structure refinements yielded good fits and low reliability factors ($R_{wp} =$ 9.164%, Supplementary Fig. 5b, Supplementary Table 5). The bond valence sums of all the cations and anions at all the sites are consistent with the formal charges (Supplementary Table 5). The refined occupancy factor of O4 atom was 0.957(14), from which the bulk water content *x* in $Ba_2LuAlO_5 \cdot x\ D_2O$ is calculated to be $x = 0.479(7)$, indicating the chemical formula $Ba_2LuAlO_{4.52}(OD)_{0.96}$ [$= Ba_2LuAlO_{4.522(7)}(OD)_{0.957(14)} = Ba_2LuAlO_5 \cdot 0.479(7)\ D_2O = Ba_2LuAlD_{0.957(14)}O_{5.479(7)}$]. This value is consistent with that from TG measurements $x = 0.50$ (Supplementary Fig. 6), indicating that most of the water is incorporated in bulk $Ba_2LuAlO_{4.522(7)}(OD)_{0.957(14)}$. These results validate the refined crystal structure of $Ba_2LuAlO_{4.522(7)}(OD)_{0.957(14)}$ at 5 K.

Crystal structures of dry, hydrated, and as-prepared Ba_2LuAlO_5. Dry Ba_2LuAlO_5, hydrated $Ba_2LuAlO_5 \cdot x\ D_2O$, and as-prepared Ba_2LuAlO_5 samples have a hexagonal perovskite-related structure with cubic close-packed BaO_3 (c) layers ($(Ba1)(O1)_3$ and $(Ba3)(O2)_3$ layers) and intrinsically oxygen-deficient hexagonal close-packed $BaO_{1+\varepsilon}$ (h′) layer ($(Ba2)(O3)(O4)_\varepsilon$ layer) in the sequence of $(ccch')_2$, where ε is the occupancy factor of O4 atom (Fig. 2 and Supplementary Fig. 3). The structure of dry and as-prepared Ba_2LuAlO_5 consists of LuO_6 octahedra, AlO_4 tetrahedra, and Ba cations, whereas the structure of hydrated $Ba_2LuAlO_5 \cdot x\ D_2O$ consists of LuO_6 octahedra, AlO_4 tetrahedra, Ba, interstitial oxygen O4 and D atoms. In the three samples, two LuO_6 octahedra form a bioctahedron (octahedral dimer) Lu_2O_{11} by sharing O1 atom, while two AlO_4 tetrahedra form an Al_2O_7 dimer by sharing O3 atom.

Ba_2LuAlO_5 is isostructural with β-Ba_2ScAlO_5 and hexagonal Ba_2InAlO_5[50,51]. Hereafter, the structure type of Ba_2LuAlO_5 is referred to as the β-Ba_2ScAlO_5-type. At room temperature, the lattice parameters of as-prepared Ba_2LuAlO_5 ($a = 5.9203(5)$ Å, $c = 19.7448(19)$ Å) are larger than those of β-Ba_2ScAlO_5 ($a = 5.79$ Å, $c = 19.35$ Å)[51] and Ba_2InAlO_5 ($a = 5.78$ Å, $c = 19.62$ Å)[50] due to the larger ionic radius of Lu^{3+} cation for coordination number of 6 (0.861 Å) compared with those of Sc^{3+} (0.745 Å) and In^{3+} (0.8 Å)[52]. The split sites were found for O3 and Ba2 in both dry and as-prepared Ba_2LuAlO_5, although the split sites were not considered in β-Ba_2ScAlO_5 and hexagonal Ba_2InAlO_5 in the literature[49,50]. As shown later, Ba_2LuAlO_5 exhibits high proton conductivity as well as $Ba_5Er_2Al_2ZrO_{13}$, and they have similar crystal structures, with stacking sequences $(ccch')_2$ and $(cccch')_2$, respectively (Supplementary Note 3 and Supplementary Fig. 10). Therefore, the number of h′ layers per unit length along the *c* axis of as-prepared Ba_2LuAlO_5 (0.101292(10) h′ layers Å^{-1}) is significantly larger than that of $Ba_5Er_2Al_2ZrO_{13}$ (0.081102(7) h′ layers Å^{-1}). The number of oxygen vacancies per unit volume of as-prepared Ba_2LuAlO_5 (6.6740(13) × 10^{-3} Å^{-3}) is also larger than that of $Ba_5Er_2Al_2ZrO_{13}$ (5.294(4) × 10^{-3} Å^{-3}), leading to larger amount of H_2O in hydrated $Ba_2LuAlO_5{\cdot}x\ H_2O$ ($x = 0.50$) than hydrated $Ba_5Er_2Al_2ZrO_{13}{\cdot}x\ H_2O$ ($x = 0.27$) at room temperature.

As shown in Fig. 3, XRPD patterns of Ba_2LuAlO_5 after annealing at 400 °C for 24 h in dry O_2, dry 5% H_2 in N_2, and wet air remain very similar to that of the as-prepared sample, indicating its high chemical stability. Supplementary Fig. 11 shows the XRPD patterns of Ba_2LuAlO_5 after annealing in dry CO_2 at 400 and 500 °C for 24 h, also indicating the high phase stability of Ba_2LuAlO_5, although a small amount of impurity Lu_2O_3 appeared during the CO_2 annealing (weight fraction of Lu_2O_3 in the sample during CO_2 annealing at 400 °C: 0.0057).

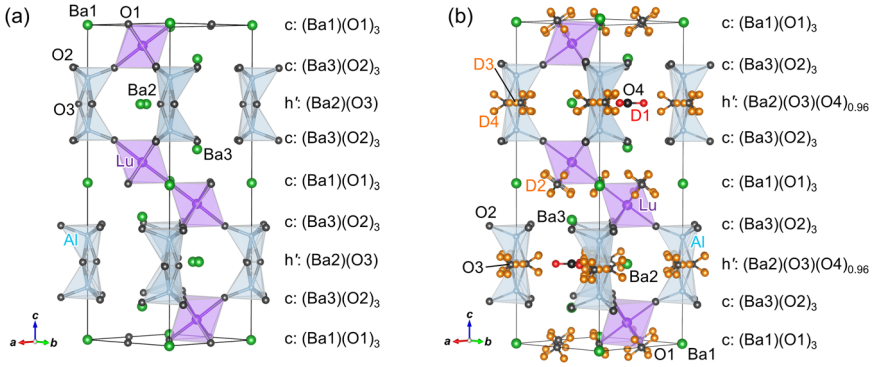

Fig. 2 Crystal structures of dry Ba_2LuAlO_5 and hydrated $Ba_2LuAlO_5 \cdot 0.48\ D_2O$. Refined crystal structures of dry **a** Ba_2LuAlO_5 and **b** hydrated $Ba_2LuAlO_5 \cdot 0.48\ D_2O$ at 5 K. Green, purple, light blue, and black balls represent Ba, Lu, Al, and O atoms, respectively. In (**b**), red balls denote D1 atoms, and orange balls represent D2, D3, and D4 atoms.

High proton conduction in Ba_2LuAlO_5. The UV-vis spectrum of Ba_2LuAlO_5 powders showed a wide optical band gap of $E_g =$ 3.99 eV, indicating that Ba_2LuAlO_5 is an electronic insulator (Supplementary Fig. 12), as supported by DFT calculations (Supplementary Fig. 13). Figure 4a shows oxygen partial pressure $P(O_2)$ dependencies of total DC electrical conductivities σ_{total} of Ba_2LuAlO_5 measured at 400 °C under dry atmosphere σ(dry) and wet condition $\sigma(H_2O)$. In the dry atmosphere, the slope of log(σ_{tot}) versus log($P(O_2)$) has a positive value in the $P(O_2)$ range from 1 to 10^{-5} atm, indicating p-type conduction. At low $P(O_2)$ range from approximately 10^{-5} to 10^{-25} atm, the conductivity σ(dry) is almost independent of $P(O_2)$, demonstrating electrolyte domain with negligible electronic conduction. Under the wet condition at 400 °C, $\sigma(H_2O)$ is almost independent of $P(O_2)$, and the ion conduction is dominant over the entire $P(O_2)$ range from 1 to 10^{-21} atm. The $\sigma(H_2O)$ value in the electrolyte domain is 35 times higher than that under the dry condition σ(dry). These observations strongly suggest that Ba_2LuAlO_5 is a proton conductor in the wet state. The proton conduction in Ba_2LuAlO_5 is further supported by the isotope effect on σ_{total}. We measured σ_{total} of Ba_2LuAlO_5 in D_2O saturated air $\sigma(D_2O)$ and H_2O saturated air $\sigma(H_2O)$ atmospheres. The conductivity ratio $\sigma(H_2O)/\sigma(D_2O)$ is in the range of 1.2–1.6 (Fig. 4b), close to the expected value of 1.414 for the Grotthuss mechanism of proton transport[53]. Similar conductivity ratio values have been reported in known proton conductors[24,54,55].

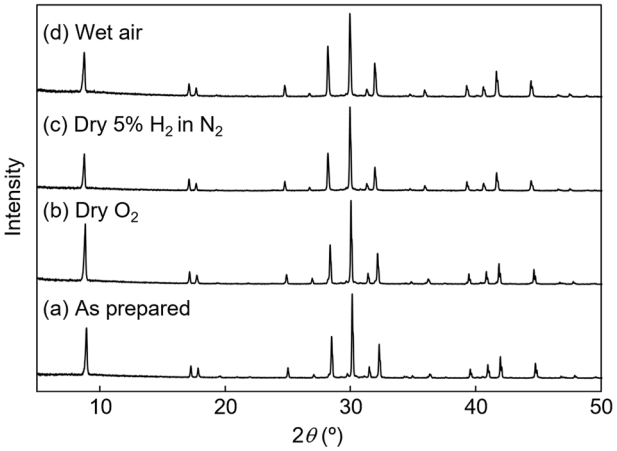

Fig. 3 High chemical stability of Ba_2LuAlO_5. X-ray powder diffraction patterns of Ba_2LuAlO_5 at room temperature. **a** As-prepared sample and samples after annealing at 400 °C in **b** dry O_2, **c** dry 5% H_2 in N_2, **d** wet air [H_2O vapor pressure of 0.021 atm] (100 mL min^{-1}) for 24 h. There are no additional peaks in these XRPD patterns after annealing, which indicates the high chemical stability of Ba_2LuAlO_5 in dry O_2, dry 5% H_2 in N_2, and wet air.

Figure 4c shows the Arrhenius plots of total DC electrical conductivity σ_{total} of Ba_2LuAlO_5 in dry N_2 gas flow σ(dry) and wet N_2 gas flow $\sigma(H_2O)$. In the whole temperature range, $\sigma(H_2O)$ is higher than σ(dry) (e.g., 63 times higher at 300 °C). The $\sigma(H_2O)$ increases with increasing temperature from 300 to 500 °C while decreasing beyond that. This behavior is typical of known proton conductors, including $Ba_5Er_2Al_2ZrO_{13}$, which is ascribed to thermal dehydration at high temperatures[37]. Indeed, thermal dehydration of Ba_2LuAlO_5 upon heating is observed in TG measurements (Supplementary Fig. 6). We can calculate proton transport number $t_H{}^+$ and proton conductivity $\sigma_H{}^+$ assuming $t_H{}^+ = \sigma_H{}^+ / \sigma(H_2O)$ and $\sigma_H{}^+ = \sigma(H_2O) - \sigma$(dry). The obtained $t_H{}^+$ is close to unity over the whole temperature range, indicating pure proton conduction (Supplementary Fig. 14).

The bulk conductivity (σ_{bulk}) of Ba_2LuAlO_5 was investigated in dry N_2 and in H_2O saturated N_2. Figure 5b, c, Supplementary Figs. 15 and 16 show typical AC impedance spectra of Ba_2LuAlO_5. The σ_{bulk} and σ_{gb} of Ba_2LuAlO_5 were obtained by the equivalent circuit analysis (Fig. 5a; Supplementary Figs. 15a, b, 16a, b, and 17; Supplementary Note 4). As shown in Fig. 5a, the bulk conductivity in H_2O saturated N_2 (vapor pressure of 0.021 atm) $\sigma_{bulk}(H_2O)$ is higher than that in dry N_2 σ_{bulk}(dry) in the whole temperature range, indicating bulk proton conduction. For example, the $\sigma_{bulk}(H_2O)$ at 400 °C is 130 times higher than σ_{bulk}(dry).

Figure 6a compares the proton conductivities σ_H of Ba_2LuAlO_5 and other proton conductors where the definition of σ_H is described for each data in the caption of Fig. 6. Ba_2LuAlO_5 exhibits σ_H value as high as 10^{-2} S cm^{-1} at 487 °C and 1.5×10^{-3} S cm^{-1} at 232 °C. The conductivity is 4.3 times higher at 200 °C and 2.0 times higher at 400 °C than those of the cubic perovskite-type $BaZr_{0.8}Y_{0.2}O_{2.9}$[56]. The σ_H of Ba_2LuAlO_5 is even higher than that of $Ba_5Er_2Al_2ZrO_{13}$, a structurally-related oxide with intrinsically oxygen-deficient h′ layers[37]. The activation energy for proton conductivity in Ba_2LuAlO_5 is estimated to be 0.36 eV below 200 °C, which is lower than that of cubic-perovskite $BaZr_{0.8}Y_{0.2}O_{3-\delta}$ (0.47 eV) and $BaZr_{0.4}Sc_{0.6}O_{2.7}$ (0.44 eV)[24]. The proton diffusion coefficient D of Ba_2LuAlO_5 is calculated by the Nernst–Einstein equation using the proton

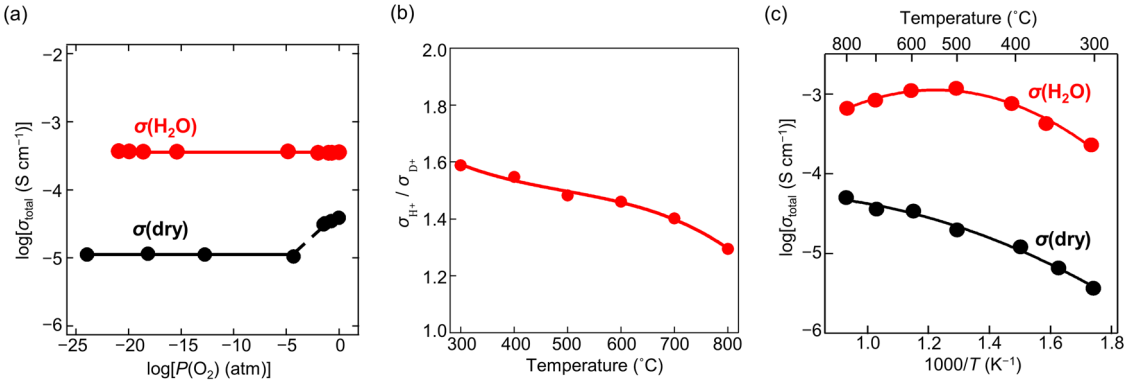

Fig. 4 Proton conduction in Ba_2LuAlO_5. **a** Oxygen partial pressure $P(O_2)$ dependencies of total DC electrical conductivity σ_{total} under dry atmospheres σ(dry) and under H_2O saturated gas $\sigma(H_2O)$. **b** Temperature dependence of the $\sigma_H{}^+/\sigma_D{}^+$ ratio in N_2 flow where the $\sigma_H{}^+$ and $\sigma_D{}^+$ are the proton and deuteron conductivities, respectively, in N_2 flow. $\sigma_H{}^+$ and $\sigma_D{}^+$ were estimated by the equations $\sigma_H{}^+ = \sigma(H_2O) - \sigma$(dry) and $\sigma_D{}^+ = \sigma(D_2O) - \sigma$(dry), respectively, where the $\sigma(H_2O)$ and $\sigma(D_2O)$ are DC electrical conductivities σ_{total} under H_2O and D_2O saturated N_2 flow, respectively. **c** Arrhenius plots of σ(dry) and $\sigma(H_2O)$ under N_2 gas flow.

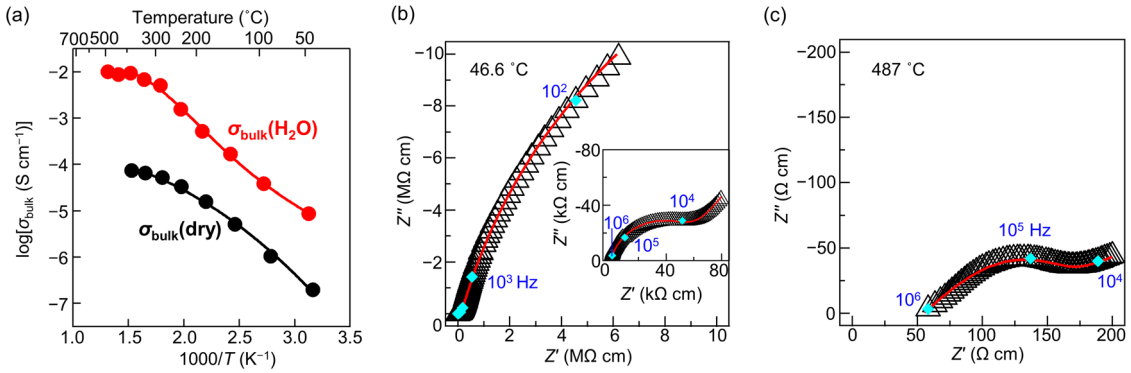

Fig. 5 High bulk conductivity of Ba_2LuAlO_5. a Arrhenius plots of bulk conductivities under dry N_2 gas flow σ_{bulk}(dry) and under wet N_2 gas flow $\sigma_{bulk}(H_2O)$ [$P(H_2O) = 0.021$ atm]. **b**, **c** Complex impedance plots of Ba_2LuAlO_5 recorded in wet N_2 gas flow at **b** 46.6 °C and **c** 487 °C. Blue numbers in panels (**b**) and (**c**) stand for the frequencies (Hz) at the points of light blue diamonds.

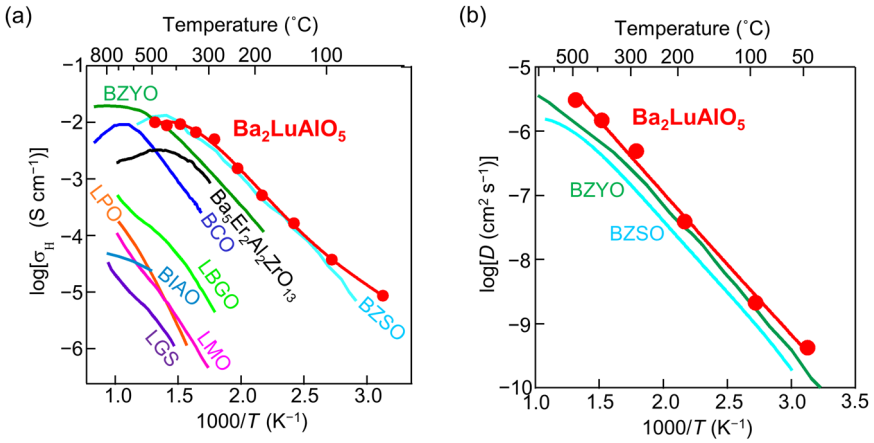

Fig. 6 Higher proton conductivity and diffusion coefficient of Ba_2LuAlO_5 compared with other leading proton conductors. a Comparison of proton conductivities σ_H of Ba_2LuAlO_5 with other proton conductors. Shown are bulk conductivity of the present Ba_2LuAlO_5 in wet N_2 and BZYO ($BaZr_{0.8}Y_{0.2}O_{2.9}$) in wet air[56], bulk conductivity of BCO ($BaCe_{0.9}Y_{0.1}O_{2.95}$) in wet air[56], total AC conductivity of BZSO ($BaZr_{0.4}Sc_{0.6}O_{2.9}$) in wet Ar[24], DC proton conductivity $\sigma_H{}^+$ of $Ba_5Er_2Al_2ZrO_{13}$[37], DC proton conductivity $\sigma_H{}^+$ of BIAO ($Ba_5In_2Al_2ZrO_{13}$)[47], bulk conductivity of LBGO ($La_{0.8}Ba_{1.2}GaO_{3.9}$) in wet air[69], DC conductivity of LPO ($La_{0.95}Sr_{0.05}PO_{3.975}$) in wet O_2[70], total AC conductivity of LMO ($La_{5.4}MoO_{11.1}$) in wet N_2[39], bulk conductivity of LGS ($La_3Ga_{5.06}Si_{0.94}O_{14}$) in wet air[71]. **b** Arrhenius plots of proton diffusion coefficients D of Ba_2LuAlO_5, BZYO ($BaZr_{0.8}Y_{0.2}O_{2.9}$)[46] and BZSO ($BaZr_{0.4}Sc_{0.6}O_{2.7}$)[24].

concentration determined by TG measurements (see details in "Methods"). As shown in Fig. 6b, Ba_2LuAlO_5 shows higher D values than the acceptor-doped perovskite-type $BaZr_{0.8}Y_{0.2}O_{2.9}$ and $BaZr_{0.4}Sc_{0.6}O_{2.7}$[24,46]. Diffusion coefficient D and activation energy for D extracted from the AIMD simulations are in good agreement with the experimental values (Supplementary Fig. 18), supporting the high D values. The acceptor doping is known to make the proton-dopant association, leading to the high apparent activation energy for D and low proton conductivity at low temperatures[46]. In sharp contrast, the present Ba_2LuAlO_5 has intrinsic oxygen vacancies without chemical doping, which leads to low activation energy and high proton conductivity at low temperatures.

We have demonstrated that Ba_2LuAlO_5 shows a high level of proton conductivity without chemical doping. This suggests that water is incorporated in the oxygen-deficient h′ layers, leading to the formation of proton carriers. TG analysis of undoped Ba_2LuAlO_5 indeed indicated a water uptake upon cooling (Supplementary Figs. 6, 19, and 20; Supplementary Table 6; Supplementary Note 5). Refined occupancy factor of oxygen atoms in the Rietveld analysis of hydrated (deuterated) $Ba_2LuAlO_{4.52}(OD)_{0.96}$ also indicated the water uptake and presence of hydroxide ions OD (Fig. 2b). The water content x in $Ba_2LuAlO_5{\cdot}x\ H_2O$ is estimated to be 0.50 at 100 °C by TG measurements, which is larger than that for $Ba_5Er_2Al_2ZrO_{13}{\cdot}x\ H_2O$ ($x = 0.27$) at the same temperature. The concentration of water relative to the number of available oxygen vacancies for $Ba_2LuAlO_5{\cdot}x\ H_2O$ ($x = 0.50$) is relatively low, 50%, compared with other proton conductors (Supplementary Fig. 21a). Meanwhile, the number of H_2O per unit volume of Ba_2LuAlO_5 ($3.3370(7) \times 10^{21}$ cm^{-3}) is relatively high as shown in Supplementary Fig. 21b. The high proton diffusion coefficient and large water concentration in Ba_2LuAlO_5 may account for the high proton conductivity.

Proton diffusion mechanism through ab initio molecular dynamics simulations of Ba_2LuAlO_5. To gain more insight into the high proton conductivity in Ba_2LuAlO_5, ab initio molecular dynamics (AIMD) simulations were performed for $Ba_2LuAlO_5 \cdot 0.125\ H_2O$ using a 2×2×2 supercell ($Ba_{32}Lu_{16}Al_{16}O_{82}H_4$). The initial structural model was made by locating two water molecules in two different h′ layers of the 2×2×2 supercell. The calculated mean square displacement (MSD) of protons is much larger than those of the other constituent atoms (Fig. 7a), indicating that proton conduction is dominant. As shown in Fig. 7b, the MSDs of protons along the a and b directions are larger than that along the

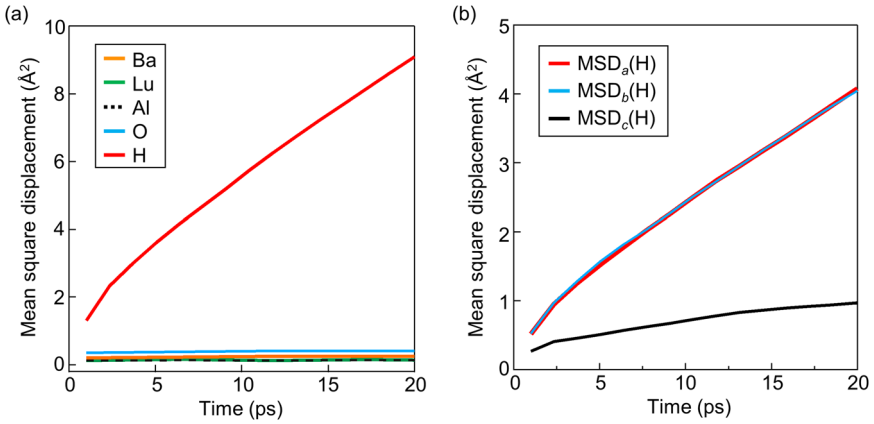

Fig. 7 Mean square displacements of $Ba_2LuAlO_5 \cdot 0.125\ H_2O$. AIMD-simulated mean square displacements (MSDs) of **a** constituent atoms and **b** protons along each direction in $Ba_2LuAlO_5 \cdot 0.125\ H_2O$ at 1473 K. In panel (**b**), red, blue, and black curves stand for the MSDs of protons along *a*, *b*, and *c* axes, respectively.

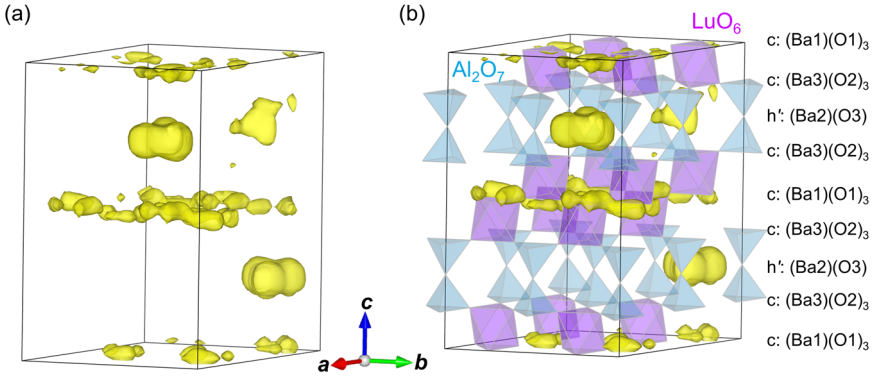

Fig. 8 Probability density distribution of protons in $Ba_2LuAlO_5 \cdot 0.125\ H_2O$. Yellow isosurface of the probability density distribution of protons at 2.0×10^{-4} Å^{-3}, which were obtained by the AIMD simulations at 1473 K. Probability density distributions **a** without and **b** with the polyhedra of AlO_4 and LuO_6.

c direction, showing the dominant two-dimensional diffusion in the *ab*-plane. The trajectory and density distribution of hydrogen atoms (Fig. 8, and Supplementary Figs. 7b and 22) indicate that two inserted water molecules dissociate into O4 atoms in the h′ layer and protons, which is consistent with the refined crystal structure (Supplementary Fig. 7a). As shown in Fig. 8 and Supplementary Fig. 22, there are two types of protons of four inserted protons: (i) two mobile protons around the $(Ba1)(O1)_3$ c layer at the interface of two LuO_6 octahedra and (ii) two trapped protons around the h′ layer. The trapped protons in the h′ layer move around an interstitial O4 oxygen atom formed by the hydration but do not migrate across the lattice. In contrast, the protons around the $(Ba1)(O1)_3$ c layer move across the lattice. Therefore, the crystal structure of Ba_2LuAlO_5 consists of (1) proton conducting c layers and (2) oxygen-deficient h′ layers that incorporate the extra oxygen atoms due to hydration. Such structural character of Ba_2LuAlO_5 enables high proton conductivity.

Conclusions

In conclusion, we have demonstrated high proton conductivity as high as 10^{-2} S cm^{-1} at 487 °C and 1.5×10^{-3} S cm^{-1} at 232 °C and high proton transport number >0.92 in the range 300–800 °C in Ba_2LuAlO_5. Structural analysis revealed that Ba_2LuAlO_5 is a hexagonal perovskite-related oxide having oxygen-deficient BaO h′ layers. The large amount of intrinsic oxygen vacancies in Ba_2LuAlO_5 allows higher water uptake of $x = 0.50$ in $Ba_2LuAlO_5 \cdot xH_2O$ than other typical perovskite and perovskite-related proton conductors, resulting in the high proton conductivity. AIMD simulations for $Ba_2LuAlO_5 \cdot 0.125\ H_2O$ have shown that protons migrate mainly near the interface of two LuO_6 octahedral layers, in contrast to the case of the hexagonal perovskite-related proton conductor $Ba_7Nb_4MoO_{20}$ where protons migrate in the oxygen-deficient c′ layer[36,57]. By modifying the chemical composition of Ba_2LuAlO_5, further improvement in conductivity could be expected[58]. For example, the hexagonal perovskite-related oxide Ba_2InAlO_5 is expected to show high conductivity as it is isostructural with Ba_2LuAlO_5. The present guidelines for the material design open new avenues for the development of high-performance proton conductors.

Methods

Synthesis and characterization. Ba_2LuAlO_5 sample was prepared by a high-temperature solid-state reaction method. The starting materials of $BaCO_3$ (99.9% purity), Lu_2O_3 (99.9% purity), and Al_2O_3 (99.9% purity) at a molar ratio of Ba:Lu:Al = 2:1:1 were mixed and ground as dried powders and as ethanol slurries for 1 h in an agate mortar, and then calcined in air at 1000 °C for 10 h to remove carbonates. The calcined materials were crushed and ground with the agate mortar, uniaxially pressed into pellets at 62–150 MPa, and then sintered in air at 1600 °C for 10 h. Parts of the sintered pellets were crushed with a tungsten carbide crusher and ground with the agate mortar into powders. Inductively coupled plasma atomic emission spectroscopy (ICP-AES) data of the Ba_2LuAlO_5 powders indicated that the chemical composition Ba:Lu:Al = 1.92(11):1.07(11):1.02(2) is in good agreement with the ratio of the nominal composition, where the numbers in the parentheses are the standard deviations. The microstructure of the as-prepared Ba_2LuAlO_5 was observed using a scanning electron microscope (SEM, Keyence VE-8800).

As-prepared pellets (approximately 5 mm in diameter, 2–3 mm in height) of Ba_2LuAlO_5 were annealed at 400 °C for 24 h under dry O_2, dry 5% H_2 in N_2, and

wet air to investigate its phase stability. The as-prepared pellets of Ba_2LuAlO_5 were also annealed under dry CO_2 flow (100 mL min^{-1}) at 400 and 500 °C for 24 h to investigate its phase stability. The annealed pellets were crushed and ground into powders, and their XRPD data were measured.

Thermogravimetric (TG) measurements of as-prepared Ba_2LuAlO_5 were carried out with NETZSCH STA 449 F3 Jupiter. The sample was heated to 800 °C at the heating rate of 10 °C min^{-1} in dry N_2 flow (vapor partial pressure $P(H_2O) < 10^{-5}$ atm) and kept for 4 h at 800 °C in order to remove water, and then the atmosphere was switched to wet N_2 flow ($P(H_2O) = 0.021$ atm) and kept for 4 h. In the cooling process, the sample was kept for 4 h at 700, 600, 500, 400, 300, 200, and 100 °C to reach equilibrium after cooling at the cooling rate of 10 °C min^{-1}. Raman spectrum of Ba_2LuAlO_5 was collected using NRS-4100 (JASCO Co.) with an excitation wavelength of 532 nm in static air. The IR spectrum of Ba_2LuAlO_5 was collected using DR PRO 410MX (JASCO Co.) in dry N_2. Ultraviolet-visible (UV-vis) diffuse reflectance spectrum of Ba_2LuAlO_5 was measured in static air at room temperature between 200 and 700 nm using a JASCO V-670 scanning double-beam spectrometer. The optical direct bandgap E_g was estimated using the Kubelka–Munk equation and a Tauc plot.

Diffraction experiments and structural analysis. A part of the as-prepared Ba_2LuAlO_5 pellet was crushed, and a single crystal of Ba_2LuAlO_5 with a size of 5 × 5 × 5 μm was picked up. Single-crystal X-ray diffraction (SCXRD) data of the as-prepared crystal were measured using a Rigaku XtaLAB Pro diffractometer (Mo $K\alpha$ radiation) at 20 °C. The crystal structure was determined by the charge flipping method using SuperFlip[59] followed by least-square refinement with SHELX (ver. 2018/3)[60]. The bond valence sum at each site was calculated using the bond-valence parameter reported in the literature[61,62]. Difference Fourier maps ($F_o - F_c$) were calculated using WinGX (ver. 2018.3)[63]. The refined crystal structures, probability density distribution of protons, and difference Fourier maps were depicted with VESTA 3[64]. The X-ray powder diffraction (XRPD) data of the as-prepared Ba_2LuAlO_5 powders were measured at 22 °C by a laboratory-based X-ray diffractometer (Bruker AXS D8 Advance) with Cu $K\alpha$ radiation at 40 kV and 40 mA (step scanning mode, 0.02° per step, counting time: 20 s per step, and 2θ range: 4–120°). Rietveld refinement was performed using the computer program Z-code[65] and crystallographic parameters obtained in the SCXRD analysis as initial parameters.

Dry Ba_2LuAlO_5 pellets were prepared by heating the as-prepared Ba_2LuAlO_5 pellets at 800 °C for 30 min in a vacuum quartz tube. The sample in the quartz tube was cooled in vacuum down to 300 °C, and then the quartz tube containing the pellets was sealed at this temperature. Hydrated (deuterated) $Ba_2LuAlO_5 \cdot x\ D_2O$ pellets were synthesized by heating the as-prepared Ba_2LuAlO_5 pellets at 800 °C for 30 min in dry N_2, cooled down to 200 °C at the cooling rate of 10 °C min^{-1} in D_2O/He flow (water vapor pressure $P(D_2O) = 0.021$ atm) and then kept at 200 °C for 2 h in the D_2O/He flow. Neutron-diffraction data of the dry Ba_2LuAlO_5 and hydrated $Ba_2LuAlO_5 \cdot x\ D_2O$ pellets were measured at 5 K with a fixed-wavelength neutron diffractometer HERMES[66] at the JRR-3 research reactor of JAEA, Tokai, Japan (wavelength = 1.34171(5) Å). The collected data were analyzed by the Rietveld method with the program RIETAN-FP[67].

Electrical conductivity measurements. The DC electrical conductivity of Ba_2LuAlO_5 was measured using sintered pellets (approximately 4.5 mm in diameter, 10–12 mm in height, relative density of 73%). Pt paste dissolved in ethanol and Pt wires were attached to both sides of the sintered pellets and heated at 500 °C for 1 h to remove the ethanol in the Pt paste. DC electrical conductivity of the Ba_2LuAlO_5 pellet was measured between 300 and 800 °C by a DC 4-probe method under N_2 flow in dry ($P(H_2O) < 10^{-5}$ atm) and wet ($P(H_2O) = 0.021$ atm and $P(D_2O) = 0.021$ atm) atmospheres (200 ml min^{-1}). Oxygen partial pressure $P(O_2)$ dependencies of the DC electrical conductivity of Ba_2LuAlO_5 were investigated at 400 °C in the dry and wet ($P(H_2O) = 0.021$ atm) atmospheres. $P(O_2)$ was controlled by O_2/N_2 or H_2/N_2 gas mixture and monitored by a YSZ oxygen sensor placed at the outlet of the apparatus.

The AC impedance spectra of Ba_2LuAlO_5 were collected in dry N_2 and wet N_2 in the temperature range of 50–500 °C. We used two sintered pellets (9.4 mm in diameter, 4.5 mm in thickness, and a relative density of 78%; and 9.9 mm in diameter, 2.6 mm in thickness, and a relative density of 59%) for the AC impedance measurements. The impedance spectra were recorded using a Solartron 1260 impedance analyzer in the frequency range of 10 MHz to 1 Hz with an applied alternating voltage of 1 V. The equivalent circuit analysis was carried out to extract the bulk conductivity σ_{bulk} at each temperature using the ZView software (Scribner Associates, Inc.).

Density functional theory calculations and ab initio molecular dynamics simulations. Density functional theory (DFT) simulations of hexagonal Ba_2LuAlO_5 (1×1×1 cell) were carried out using the Vienna Ab initio Simulation Package (VASP)[68]. We used projector augmented-wave (PAW) potentials for Ba, Lu, Al, and O atoms; the plane-wave basis sets with a cutoff of 500 eV, and the Perdew–Burke–Ernzerhof (PBE) GGA functionals. A 5×5×2 k-point mesh was used in the Monkhorst–Pack scheme. In self-consistent cycles, the total energy was minimized until the energy convergence was less than 10^{-7} eV. Lattice parameters and atomic coordinates of Ba_2LuAlO_5 were optimized for 27 models with different atomic configurations in the space groups Pm and $P2_1/m$ with a convergence condition of 0.001 eV $Å^{-1}$. The crystal parameters refined using the SCXRD data were used as initial parameters in the DFT structure optimizations.

AIMD simulations of $(Ba_2LuAlO_5 \cdot 0.125\ H_2O)_{16}$ (= $Ba_{32}Lu_{16}Al_{16}O_{80} \cdot 2\ H_2O$) were performed at 873, 1073, 1273, and 1473 K by VASP using a 2 × 2 × 1 supercell of Ba_2LuAlO_5 to investigate the proton migration. The initial structural model was made by locating two water molecules in two different h′ layers of the supercell. The geometry-optimized structure was heated from 0 K to the target temperature at a rate of 1 K fs^{-1}. The system was further equilibrated for 5 ps, and the production trajectory was accumulated for the canonical (NVT) ensemble using a Nosé thermostat for ~200 ps with the time step of 1 fs. The cutoff energy was set to 300 eV, and the reciprocal space integration was performed only at the Γ-point.

Data availability

The data that support the findings of this study are available from the corresponding author upon reasonable request.

Received: 1 July 2022; Accepted: 12 May 2023;
Published online: 06 June 2023

References

1. Goodenough, J. B. Oxide-ion conductors by design. *Nature* **404**, 821–823 (2000).
2. Skinner, S. J. & Kilner, J. A. Oxygen ion conductors. *Mater. Today* **6**, 30–37 (2003).
3. Thangadurai, V. & Weppner, W. Recent progress in solid oxide and lithium ion conducting electrolytes research. *Ionics* **12**, 81–92 (2006).
4. Aguadero, A. et al. Materials development for intermediate-temperature solid oxide electrochemical devices. *J. Mater. Sci.* **47**, 3925–3948 (2012).
5. Mahato, N., Banerjee, A., Gupta, A., Omar, S. & Balani, K. Progress in material selection for solid oxide fuel cell technology: a review. *Prog. Mater. Sci.* **72**, 141–337 (2015).
6. Wachsman, E. D. & Lee, K. T. Lowering the temperature of solid oxide fuel cells. *Science* **334**, 935–939 (2011).
7. Duan, C. et al. Readily processed protonic ceramic fuel cells with high performance at low temperatures. *Science* **349**, 1321–1326 (2015).
8. Perrichon, A. et al. Local coordination environments and vibrational dynamics of protons in hexagonal and cubic Sc-doped $BaTiO_3$ proton-conducting oxides. *J. Phys. Chem. C* **124**, 8643–8651 (2020).
9. Norby, T. Solid-state protonic conductors: principles, properties, progress and prospects. *Solid State Ionics* **125**, 1–11 (1999).
10. Anilkumar, G. M., Nakazawa, S., Okubo, T. & Yamaguchi, T. Proton conducting phosphated zirconia-sulfonated polyether sulfone nanohybrid electrolyte for low humidity, wide-temperature PEMFC operation. *Electrochem. Commun.* **8**, 133–136 (2006).
11. Baranov, A. I., Shuvalov, L. A. & Shchagina, N. M. Superion conductivity and phase-transitions in $CsHSO_4$ and $CsHSeO_4$ crystals. *JETP Lett.* **36**, 381–384 (1982).
12. Yang, B., Kannan, A. M. & Manthiram, A. Stability of the dry proton conductor CsHSO4 in hydrogen atmosphere. *Mater. Res. Bull.* **38**, 691–698 (2003).
13. Seen, A. J. Nafion: an excellent support for metal-complex catalysts. *J. Mol. Catal. A Chem.* **177**, 105–112 (2001).
14. Verbraeken, M. C., Cheung, C., Suard, E. & Irvine, J. T. S. High H^- ionic conductivity in barium hydride. *Nat. Mater.* **14**, 95–100 (2015).
15. Fukui, K., Iimura, S., Iskandarov, A., Tada, T. & Hosono, H. Room-temperature fast H^- conduction in oxygen-substituted lanthanum hydride. *J. Am. Chem. Soc.* **144**, 1523–1527 (2022).
16. Takeiri, F. et al. Hydride-ion-conducting K_2NiF_4-type Ba–Li oxyhydride solid electrolyte. *Nat. Mater.* **21**, 325–330 (2022).
17. Kobayashi, Y. et al. An oxyhydride of $BaTiO_3$ exhibiting hydride exchange and electronic conductivity. *Nat. Mater.* **11**, 507–511 (2012).
18. Iwahara, H., Asakura, Y., Katahira, K. & Tanaka, M. Prospect of hydrogen technology using proton-conducting ceramics. *Solid State Ionics* **168**, 299–310 (2004).
19. Nakamura, T. et al. Energy efficiency of ionic transport through proton conducting ceramic electrolytes for energy conversion applications. *J. Mater. Chem. A* **6**, 15771–15780 (2018).
20. Norby, T. The promise of protonics. *Nature* **410**, 877–878 (2001).
21. Kitamura, N., Amezawa, K., Tomii, Y. & Yamamoto, N. Protonic conduction in rare earth orthophosphates with the monazite structure. *Solid State Ionics* **162–163**, 161–165 (2003).
22. Matsumoto, H., Kawasaki, Y., Ito, N., Enoki, M. & Ishihara, T. Relation between electrical conductivity and chemical stability of $BaCeO_3$-based proton

conductors with different trivalent dopants. *Electrochem. Solid-State Lett.* **10**, B77 (2007).
23. Malavasi, L., Fisher, C. A. J. & Islam, M. S. Oxide-ion and proton conducting electrolyte materials for clean energy applications: structural and mechanistic features. *Chem. Soc. Rev.* **39**, 4370–4387 (2010).
24. Hyodo, J., Kitabayashi, K., Hoshino, K., Okuyama, Y. & Yamazaki, Y. Fast and stable proton conduction in heavily scandium-doped polycrystalline barium zirconate at intermediate temperatures. *Adv. Energy Mater.* **10**, 2000213 (2020).
25. Hossain, M. K. et al. Recent progress in barium zirconate proton conductors for electrochemical hydrogen device applications: a review. *Ceram. Int.* **47**, 23725–23748 (2021).
26. Fop, S. Solid oxide proton conductors beyond perovskites. *J. Mater. Chem. A* **9**, 18836–18856 (2021).
27. Matsumoto, H., Nomura, I., Okada, S. & Ishihara, T. Intermediate-temperature solid oxide fuel cells using perovskite-type oxide based on barium cerate. *Solid State Ionics* **179**, 1486–1489 (2008).
28. Katahira, K., Kohchi, Y., Shimura, T. & Iwahara, H. Protonic conduction in Zr-substituted $BaCeO_3$. *Solid State Ionics* **138**, 91–98 (2000).
29. Bohn, H. G., Schober, T., Mono, T. & Schilling, W. The high temperature proton conductor $Ba_3Ca_{1.18}Nb_{1.82}O_{9-\delta}$. I. Electrical conductivity. *Solid State Ionics* **117**, 219–228 (1999).
30. Gilardi, E. et al. Effect of dopant-host ionic radii mismatch on acceptor-doped barium zirconate microstructure and proton conductivity. *J. Phys. Chem. C* **121**, 9739–9747 (2017).
31. Yang, L. et al. Enhanced sulfur and coking tolerance of a mixed ion conductor for SOFCs: $BaZr_{0.1}Ce_{0.7}Y_{0.2-x}Yb_xO_{3-\delta}$. *Science* **326**, 126–129 (2009).
32. Sakthivel, M. & Weppner, W. Application of layered perovskite type proton conducting $KCa_2Nb_3O_{10}$ in H_2 sensors: Pt particle size and temperature dependence. *Sens. Actuators B Chem.* **125**, 435–440 (2007).
33. Yashima, M. et al. High oxide-ion conductivity through the interstitial oxygen site in $Ba_7Nb_4MoO_{20}$-based hexagonal perovskite related oxides. *Nat. Commun.* **12**, 556 (2021).
34. Thangadurai, V. & Weppner, W. $AA'_2M_3O_{10}$ (A = K, Rb, Cs; A′ = Ca; M = Nb) layered perovskites: low-temperature proton conductors in hydrogen atmospheres. *J. Mater. Chem.* **11**, 636–639 (2001).
35. Tarasova, N., Animitsa, I. & Galisheva, A. Electrical properties of new protonic conductors $Ba_{1+x}La_{1-x}InO_{4-0.5x}$ with Ruddlesden-Popper structure. *J. Solid State Electrochem.* **24**, 1497–1508 (2020).
36. Fop, S. et al. High oxide ion and proton conductivity in a disordered hexagonal perovskite. *Nat. Mater.* **19**, 752–757 (2020).
37. Murakami, T., Hester, J. R. & Yashima, M. High proton conductivity in $Ba_5Er_2Al_2ZrO_{13}$, a hexagonal perovskite-related oxide with intrinsically oxygen-deficient layers. *J. Am. Chem. Soc.* **142**, 11653–11657 (2020).
38. Nigara, Y., Yashiro, K., Kawada, T. & Mizusaki, J. The atomic hydrogen permeability in $(CeO_2)_{0.85}(CaO)_{0.15}$ at high temperatures. *Solid State Ionics* **145**, 365–370 (2001).
39. López-Vergara, A. et al. Effect of preparation conditions on the polymorphism and transport properties of $La_{6-x}MoO_{12-\delta}$ ($0 \le x \le 0.8$). *Chem. Mater.* **29**, 6966–6975 (2017).
40. Yashima, M. et al. Diffusion path and conduction mechanism of protons in hydroxyapatite. *J. Phys. Chem. C* **118**, 5180–5187 (2014).
41. Spesivtseva, I. V., Kochetova, N. A., Gorbunova, E. M. & Animitsa, I. E. Solid solutions of $Ba_2(In_{1-x}Al_x)_2O_5$: structural evolution and hydration processes. *Russ. J. Phys. Chem. A* **85**, 1689–1694 (2011).
42. Haugsrud, R. & Norby, T. Proton conduction in rare-earth ortho-niobates and ortho-tantalates. *Nat. Mater.* **5**, 193–196 (2006).
43. Amsif, M. et al. Mo-substituted lanthanum tungstate $La_{28-y}W_{4+y}O_{54+\delta}$: a competitive mixed electron-proton conductor for gas separation membrane applications. *Chem. Mater.* **24**, 3868–3877 (2012).
44. Hermet, J., Torrent, M., Bottin, F., Dezanneau, G. & Geneste, G. Hydrogen diffusion in the protonic conductor $BaCe_{1-x}Gd_xO_{3-x/2}$ from density functional theory. *Phys. Rev. B Condens. Matter Mater. Phys.* **87**, 104303 (2013).
45. Stokes, S. J. & Islam, M. S. Defect chemistry and proton-dopant association in $BaZrO_3$ and $BaPrO_3$. *J. Mater. Chem.* **20**, 6258–6264 (2010).
46. Yamazaki, Y. et al. Proton trapping in yttrium-doped barium zirconate. *Nat. Mater.* **12**, 647–651 (2013).
47. Andreev, R., Korona, D., Anokhina, I. & Animitsa, I. Proton and oxygen-ion conductivities of hexagonal perovskite $Ba_5In_2Al_2ZrO_{13}$. *Materials* **15**, 3944 (2022).
48. Saito, K., Fujii, K. & Yashima, M. Oxide-ion and proton conductivity of the ordered perovskite $BaY_{1/3}Ga_{2/3}O_{2.5}$. *J. Solid State Chem.* **32**, 751 (2021).
49. Shpanchenko, R. V. et al. Structural study of the new complex oxides $Ba_{5-y}Sr_yR_{2-x}Al_2Zr_{1+x}O_{13+x/2}$ (R= Gd-Lu, Y, Sc). *J. Solid State Chem.* **118**, 180–192 (1995).
50. Müller-Buschbaum, H. & Abed, M. Ba_2InAlO_5: A New Structure Type of Oxometallates of the Formula $A_2M_2O_5$. *Zeitschrift fuer Anorg. und Allg. Chemie* **591**, 174–180 (1990).
51. Shpanchenko, R. V., Antipov, E. V., Lykova, L. N. & Kovba, L. M. Crystal-structure of beta-Ba_2ScAlO_5. *Vestn. Mosk. Univ. SERIYA 2 KHIMIYA* **31**, 555–558 (1990).
52. Shannon, R. D. Revised effective ionic radii and systematic studies of interatomic distances in halides and chalcogenides. *Acta Crystallogr. A Cryst. Phys. Diffr. Theor. Gen. Crystallogr.* **32**, 715–767 (1976).
53. Nowick, A. S. & Vaysleyb, A. V. Isotope effect and proton hopping in high-temperature protonic conductors. *Solid State Ionics* **97**, 17–26 (1997).
54. Rahman, S. M. et al. Proton conductivity of hexagonal and cubic $BaTi_{1-x}Sc_xO_{3-\delta}$ ($0.1 \le x \le 0.8$). *J. Chem. Soc. Dalt. Trans.* **43**, 15055–15064 (2014).
55. Ruf, M. et al. Transport properties and oxidation and hydration kinetics of the proton conductor Mo doped $Nd_{5.5}WO_{11.25-\delta}$. *J. Mater. Chem. A* **2**, 18539–18546 (2014).
56. Kreuer, K. D. Proton-conducting oxides. *Annu. Rev. Mater. Res.* **33**, 333–359 (2003).
57. Yasui, Y. et al. Hidden chemical order in disordered $Ba_7Nb_4MoO_{20}$ revealed by resonant X-ray diffraction and solid-state NMR. *Nat. Commun.* **14**, 2337 (2023).
58. Murakami, T., Avdeev, M., Morikawa, R., Hester, J. R. & Yashima, M. High proton conductivity in β-Ba_2ScAlO_5 enabled by octahedral and Intrinsically oxygen-deficient layers. *Adv. Funct. Mater.* **33**, 2206777 (2023).
59. Palatinus, L. & Chapuis, G. SUPERFLIP: a computer program for the solution of crystal structures by charge flipping in arbitrary dimensions. *J. Appl. Crystallogr.* **40**, 786–790 (2007).
60. Sheldrick, G. M. Crystal structure refinement with SHELXL. *Acta Crystallogr. C Struct. Chem.* **71**, 3–8 (2015).
61. Brown, I. D. & Altermatt, D. Bond-valence parameters obtained from a systematic analysis of the Inorganic Crystal Structure Database. *Acta Crystallogr. B* **41**, 244–247 (1985).
62. Brese, N. E. & O' Keeffe, M. Bond-valence parameters for solid. *Acta Crystallogr. B* **47**, 192–197 (1991).
63. Farrugia, L. J. WinGX and ORTEP for Windows: an update. *J. Appl. Crystallogr.* **45**, 849–854 (2012).
64. Momma, K. & Izumi, F. VESTA 3 for three-dimensional visualization of crystal, volumetric and morphology data. *J. Appl. Crystallogr.* **44**, 1272–1276 (2011).
65. Oishi, R. et al. Rietveld analysis software for J-PARC. *Nucl. Instrum. Methods Phys. Res. A* **600**, 94–96 (2009).
66. Ohoyama, K. et al. The new neutron powder diffractometer with a multi-detector system for high-efficiency and high-resolution measurements. *Jpn. J. Appl. Phys.* **37**, 3319–3326 (1998).
67. Izumi, F. & Momma, K. Three-dimensional visualization in powder diffraction. *Solid State Phenom.***130**, 15–20 (2007).
68. Kresse, G. & Joubert, D. From ultrasoft pseudopotentials to the projector augmented-wave method. *Phys. Rev. B Condens. Matter Mater. Phys.* **59**, 1758–1775 (1999).
69. Li, S., Schönberger, F. & Slater, P. $La_{1-x}Ba_{1+x}GaO_{4-x/2}$: a novel high temperature proton conductor. *Chem. Commun.* 2694–2695 (2003).
70. Amezawa, K., Maekawa, H., Tomii, Y. & Yamamoto, N. Protonic conduction and defect structures in Sr-doped $LaPO_4$. *Solid State Ionics* **145**, 233–240 (2001).
71. Bjørheim, T. S. & Haugsrud, R. Proton transport properties of the $RE_3Ga_5MO_{14}$ (RE = La, Nd and M = Si, Ti, Sn) langasite family of oxides. *Solid State Ionics* **275**, 29–34 (2015).

Acknowledgements

We would like to express special thanks to Dr. Y. Yasui for the valuable discussion on the crystal structure analysis. We would like to thank Mr. M. Ohkawara for his assistance in the neutron diffraction experiments with HERMES, which were carried out by the projects (22603, 22610, 22614, 21578). We also thank Shin-Etsu Chemical Co. Ltd. and Kojundo Chemical Laboratory Co. Ltd. for providing raw materials and arranging ICP-AES measurements. We acknowledge Dr. M. Tada for carrying out the Raman measurements. We also acknowledge JASCO Co. for measuring IR data. This work was supported by Grant-in-Aid for Scientific Research (KAKENHI, JP19H00821, JP19K23647, JP21K14701, JP21K18182, JP21H03732, JP22H04504, JP22H05145, JP23K04887, JP23H04618) from the Ministry of Education, Culture, Sports, Science and Technology of Japan, Adaptable and Seamless Technology Transfer Program through Target-driven R&D (A-STEP) from the Japan Science and Technology Agency (JST) Grant Number JPMJTR22TC, JSPS Core-to-Core Programs, A Advanced Research Networks (Solid Oxide Interfaces for Faster Ion Transport; Mixed Anion Research for Energy Conversion [JPJSCCA20200004]), JST FOREST (Grant No. JPMJFR202V), and the Institute for Solid State Physics, the University of Tokyo. Test experiments were carried out by project Nos. 2020L801, 2021B1826, and 2021G615. T.M. acknowledges support from the Izumi Science and Technology Foundation, the Iwatani Naoji Foundation, the Daiichi Kigenso Kagaku Kogyo Co., Ltd., the Hattori Hokokai Foundation, and Iketani Science and Technology Foundation. M.A. acknowledges the support from JSPS: Invitational Fellowship for Research in Japan L19533.

Author contributions

M.Y., R.M., and T.M. designed the research. K.F., Y.I., and Y.N. collected neutron-diffraction data. R.M. and T.M. prepared the samples and measured the X-ray diffraction data, electrical conductivity, and TG data. M.A. performed AIMD simulations. K.F. and R.M. measured and analyzed the single-crystal X-ray diffraction data. R.M., M.A., K.F., and M.Y. made the figures and tables. M.Y. and R.M. wrote and edited the manuscript. All the authors read the manuscript.

Competing interests

The authors declare no competing interests.

Additional information

Supplementary information The online version contains supplementary material available at https://doi.org/10.1038/s43246-023-00364-5.

Correspondence and requests for materials should be addressed to Masatomo Yashima.

Peer review information *Communications Materials* thanks Sacha Fop and the other anonymous reviewer(s) for their contribution to the peer review of this work. Primary handling editors: Jet-Sing Lee and John Plummer. A peer review file is available.